Low thermal conductivity in heteroanionic materials with layers of homoleptic polyhedra

Chi Zhang[†], Jiangang He[†], Rebecca McClain[‡], Hongyao Xie[‡], Songting Cai[†], Lauren N. Walters[†], Jiahong Shen[†], Fenghua Ding[‡], Xiuquan Zhou[⊥], Christos D. Malliakas[‡], James M. Rondinelli[†], Mercouri G. Kanatzidis[‡], Chris Wolverton[†], Vinayak P. Dravid[*,†,§], Kenneth R. Poeppelmeier[*,‡]

[†] Department of Materials Science and Engineering, Northwestern University, Evanston, IL, 60208, USA

[‡] Department of Chemistry, Northwestern University, Evanston, IL, 60208, USA

[§] The NU*ANCE* Center, Northwestern University, Evanston, IL, 60208, USA

[⊥] Materials Science Division, Argonne National Laboratory, Lemont, IL, 60439, USA

ABSTRACT: Although BiAgOSe, an analogue of a well-studied thermoelectric material BiCuOSe, is thermodynamically stable, its synthesis is complicated by the low driving force of formation from the stable binary and ternary intermediates. Here we have developed a "subtraction strategy" to suppress byproducts and produce pure phase BiAgOSe using hydrothermal methods. Electronic structure calculations and optical characterization show that BiAgOSe is an indirect bandgap semiconductor with a bandgap of 0.95 eV. The prepared sample exhibits lower lattice thermal conductivities (0.61 $W \cdot m^{-1} \cdot K^{-1}$ at room temperature and 0.35 $W \cdot m^{-1} \cdot K^{-1}$ at 650 K) than BiCuOSe. Lattice dynamical simulations and variable temperature diffraction measurements demonstrate that the low lattice thermal conductivity arises from both the low sound velocity and high phonon–phonon scattering rates in BiAgOSe. These in turn result primarily from the soft Ag–Se bonds in the edge-sharing $AgSe_4$ tetrahedra and large sublattice mismatch between the quasi-two-dimensional $[Bi_2O_2]^{2+}$ and $[Ag_2Se_2]^{2-}$ layers. These results highlight the advantages of manipulating the chemistry of homoleptic polyhedra in heteroanionic compounds for electronic structure and phonon transport control.

Introduction

Crystalline solids with ultralow thermal conductivity are not only of fundamental interest in basic science, but also find applications in refractory materials[1], thermal barrier coatings[2,3], thermal data-storage devices[4], and high-performance thermoelectrics[5]. Among these, thermoelectric materials have drawn broad attention because the thermoelectric effect enables direct conversion between thermal and electrical energies, and are therefore treated as candidates for clean power generation as well as waste heat recycling.[6–9] Therefore, it is of economic and environmental importance to discover and develop crystalline solids with low thermal conductivity for the generation, conservation, and efficient management of thermal energy.[10,11]

Decades of studies on thermoelectric materials have shown that semiconductors with low sound velocity[12–14] or strong phonon scattering[15,16] exhibit low lattice thermal conductivities (κ_L)[17], which are usually compounds with heavy constituent atoms or complex structure.[18] Previous studies show that heteroanionic materials containing an ionic anion and a more covalent anion exhibit complex layered structures with homoleptic polyhedra,[19–22] where each anion is coordinated by its corresponding hard or soft cation following Hard-Soft Acid-Base (HSAB) theory[23]. The interface interactions between the adjacent layers in these materials induce large lattice anharmonicity, and consequently can promote ultralow intrinsic lattice thermal conductivity.[24–26] Guided by these concepts, many semiconductors with ultralow κ_L have been discovered.[27]

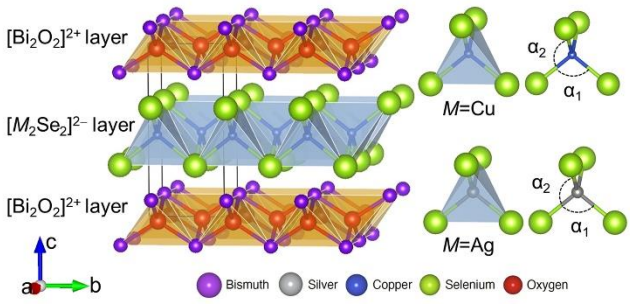

Figure 1. Crystal structures of the layered bismuth oxyselenide Bi*M*OSe (*M* = Cu, Ag) family. $[Bi_2O_2]^{2+}$ and $[M_2Se_2]^{2-}$ layers extend in the *a*-*b* plane and are formed by OBi_4 and MSe_4 tetrahedra.

BiCuOSe is among the aforementioned heteroanionic semiconductors known to have an ultralow κ_L (0.62–1.28 $W \cdot m^{-1} \cdot K^{-1}$ at room temperature and 0.45–0.76 $W \cdot m^{-1} \cdot K^{-1}$ at 650 K[28–34]),

making it one of the best thermoelectric materials at moderate temperatures. BiCuOSe crystallizes in the ZrSiCuAs-type structure (space group $P4/nmm$), which is adopted by many heteroanionic compounds that follow HSAB theory.[35,36] As such a compound, BiCuOSe is comprised of layers of edge sharing bismuth oxide (OBi_4) and of edge-sharing copper chalcogenide tetrahedra ($CuSe_4$). These two-dimensional sheets of $[Bi_2O_2]^{2+}$ and $[Cu_2Se_2]^{2-}$ alternate and stack perpendicular to the *c*-axis, as shown in Figure 1.[30,37] Earlier studies suggested that the large anharmonicity originating from the lone-pair electrons of Bi^{3+} leads to the low κ_L.[29] However, a more recent study reported that a very low frequency vibrational mode with Cu character also plays an important role in suppressing heat transfer through the lattice.[38]

The analogue, BiAgOSe, is predicted to be both thermodynamically and lattice dynamically stable in the ZrSiCuAs-type structure according to density functional theory (DFT) calculations.[39–41] Therefore it is expected to exhibit low thermal conductivity as well. A previous study by Farooq et al. showed that a small percentage of Ag substitutions for Cu could indeed lower κ_L, but more extensive doping has not been reported.[42] It is anticipated that the fully substituted compound will exhibit lower lattice thermal conductivity.[43] However, the traditional solid-state synthetic approach that is effective for BiCuOSe and other compounds in this family, such as BiCuO*Ch* (*Ch*=S, Te)[44–47] and CeAgOS[48], does not produce BiAgOSe, see Table S1. As a matter of fact, the synthesis of this class of materials is difficult[39,49] because of the formation of homoanionic phases as intermediates according to HSAB theory;[50] if those intermediates are highly stable, the extremely low formation driving force will impede the further reaction to the desired heteroanionic materials.[51,52]

Therefore, the preparation of heteroanionic compounds calls for alternative synthesis methods; hydrothermal synthesis is a promising approach because of lower reaction temperatures and shorter reaction times.[53–56] For example, BiAgOS[49], BiCuOS[57] and BiCuOSe[58] have all been successfully synthesized hydrothermally, consistent with DFT calculations and electrochemical stability diagrams describing product yields.[59] BiAgOSe has been synthesized by ion exchange of Cu^+ with Ag^+ in a $AgNO_3$ solution.[39] However, it has not been obtained hydrothermally as a pure phase, limiting further studies on its transport properties.

This work investigates the hydrothermal synthesis and physical properties of BiAgOSe. We have successfully synthesized pure BiAgOSe with an optimized hydrothermal method based on a three-step procedure, in which the side-reaction that consumes most of formation energy is suppressed. The synthetic strategy we have developed provides insight into future hydrothermal synthesis design of heteroanionic compounds with low energetic driving forces. Advanced microstructural characterization, electronic and phonon band dispersions, thermal stability and thermal conductivity of BiAgOSe are also reported. We address how the complete substitution of Cu by Ag in BiCuOSe alters the electronic structure both theoretically and experimentally. The prepared sample of BiAgOSe exhibits an extremely low thermal conductivity. Our DFT calculations, along with the measured atomic displacement parameters, indicate that the low κ_L is due to the low sound velocity and high phonon–phonon scattering rates, which primarily originate from the flexible Ag–Se bonds and large sublattice mismatch between layers.

Experimental Section

Synthesis. BiAgOSe crystals were synthesized by the hydrothermal reaction of Bi_2O_3 (99.99%, Alfa Aesar), elemental Se (99.5+%, Aldrich), and elemental Ag (99.9%, Alfa Aesar). 0.6 mmol of Bi_2O_3 and 0.96 mmol of Ag and 1.20 mmol of Se, 7.5 mmol NaOH and 2 ml distilled water were charged into a 3 × 1.75 in. rectangular Teflon pouch. Teflon pouches were placed in a 125 mL poly(tetrafluoroethylene) (PTFE) Teflon-lined pressure vessel (Parr Instruments), which was then filled with 50 mL of distilled water as backfill. The pressure vessel was then sealed and heated to 423 K at a controlled temperature ramp of 1 K/min. This process was followed by a temperature increase to 513 K over 5 hours at 0.3 K/min. The maximum temperature was held constant for 48 hours, followed by subsequent cooling to room temperature at 6 K/h. The polycrystalline products were recovered by filtration, and finally rinsed with deionized water. The solid products were leached with 1 M HCl for two hours to remove unreacted reagent Bi_2O_3. Then the remaining products were put back into a Teflon pouch along with 7.5 mmol NaOH and 2 ml distilled water and the hydrothermal process was repeated. The polycrystalline products were recovered by filtration, and finally rinsed with deionized water.

Powder X-ray Analysis. Phase fraction and reaction completeness were verified with laboratory powder X-ray diffraction (PXRD) patterns collected over a 2Θ range of 20–70° (Cu-radiation) on a Rigaku Ultima IV X-ray diffractometer under ambient condition. Phase fractions for all samples were obtained by analyzing the PXRD data with the General Structure Analysis System II package.[60] Variable-temperature synchrotron X-ray diffraction was conducted at 11-BM at the Advanced Photon Source in Argonne National Laboratory. BiAgOSe and BiCuOSe powders were sieved and loaded into a carbon coated 0.3 mm o.d. quartz capillary. Capillaries were subsequently flame sealed under vacuum (ca. 3×10^{-3} mbar). Diffraction patterns were collected at a wavelength of 0.41267 Å and at temperatures 300 K, 373K, 473K, 573K, 623K and 673K. Powder diffraction data were analyzed using Rietveld refinement and sequential refinements in Jana2006.

The atomic displacement parameters (ADP) were refined from the diffraction pattern. The slope of each element's ADP data versus temperature can be used to estimate the Einstein temperature and Debye temperature.[61] According to the structure feature, silver atoms were treated with the Einstein model.[38] Therefore eq. 1 has been used to determine the Einstein temperature of the silver atoms:[62]

$$U_{iso} = h^2T/(mk_B\Theta_E^2 4\pi^2) \quad (1)$$

where h and k_B are the Planck and Boltzmann constants, m is the reduced mass and Θ_E is the Einstein temperature of the oscillator. Vibrational frequency ν is related to Θ_E by $\nu = k_B\Theta_E/h$. As a contrast, Bi and Se atoms are considered to form the stiff framework. Therefore, their Debye temperature Θ_D has been determined using the eq. 2:

$$U_{iso} = [3h^2/(mk_B\Theta_D^2 4\pi^2]T \quad (2)$$

The average velocity of sound in the Debye model is given by:

$$v_s = \Theta_D 2\pi k_B/[h[6\pi^2 n]^{1/3}] \quad (3)$$

where n is the number of atoms per unit volume.

Scanning/Transmission Electron Microscopy (S/TEM) Characterization. Electron-beam-transmitted TEM specimens were prepared by ultramicrotomy. BiAgOSe crystals were embedded in resin. Then, several sections containing BiAgOSe particles with 80~90 nm thickness were obtained. High-resolution transmission electron microscopy (HRTEM) images and selected-area electron diffraction (SAED) patterns were obtained using a JEOL Grand ARM operated at 300 kV, and atomic-resolution annular bright-field (ABF) (11–22 mrad of collection angle) and high-angle annular dark-field (HAADF) (90–200 mrad) scanning transmission electron microscopy (STEM) images were acquired using a Cs-corrected JEOL ARM 200CF operated at 200 kV. The multislice simulation was conducted with software Dr. Probe under 200 kV, a thickness of 25.53 nm, a convergence angle of 24 mrad, and a defocus of 0 nm, using frozen lattice configurations and the number of variants per slice set to 10.

Thermal Transport Property Measurement. To prepare pellets for thermal transport property measurement, the hydrothermally synthesized fine powders were cold pressed into pellets (12.7 mm in diameter) and densified using the spark plasma sintering technique (SPS-211LX, Fuji Electronic Industrial Co. Ltd.) under vacuum, at 573 K with a uniaxial compressive pressure (40 MPa) for 6 min, followed by a second-round spark plasma sintering at 648 K under a uniaxial compressive pressure (40 MPa) for 6 min. The thermal diffusivity (D) was measured by a laser flash analysis instrument (LFA-457, Netzsch, Germany) under N_2 flow. Samples were finally processed into pellets with dimensions ~6 × 6 × 2 mm^3. The measured density is 90.7% of the theoretical value. The thermal conductivities were calculated based on the equation $\kappa = D \cdot C_p \cdot \rho$, where D is the thermal diffusivity, C_p is the specific heat, and ρ is the density. The specific heats of the samples were estimated by $C_p = 3R/M$, where R is the ideal gas constant and M is the average molar mass of each element. The densities of the samples were calculated by their dimensions and masses. The uncertainties of diffusivity measurement and density measurement are ~5% and ~5%, respectively. Therefore, the uncertainty of the thermal transport measurements can be estimated to be ~10%.

DFT calculations. All DFT calculations were performed using the Vienna ab Initio Simulation Package (VASP).[63,64] The PBEsol version of the exchange-correlation functional[65], projector-augmented wave method[66] and the plane wave basis sets with an energy cutoff of 520 eV were all used for structure relaxation, electronic structures, and second and third-order force constants calculations. Spin-orbit coupling was considered for all calculations related to energetics and reaction driving forces, as has been shown to be necessary in previous works.[59,67] The crystal orbital Hamilton population analysis was performed using the Lobster code.[68] The second-order force constants were computed by using the finite displacement method as implemented in the Phonopy package.[69] Supercells with size of 4 × 4 × 2 and an atomic displacement of 0.01 Å were utilized. The third-order force constants were computed by using the third-order.py[70] with 2 × 2 × 1 supercells, including third-neighbor interactions. Lattice thermal conductivities were calculated by solving the Boltzmann transport equation for phonons, as implemented in the ShengBTE code.[71] Grüneisen parameters were computed using the force constants of the equilibrium volume (V_o), 2%V_o, and −2%V_o.

Results and Discussion

Optimized Hydrothermal Synthesis

The selection of reactants is a key step in any hydrothermal synthesis, and it will affect the composition and morphology of products. In the reaction to synthesize BiAgOSe, we selected Bi_2O_3, Ag and Se as starting materials after careful consideration. Less soluble Bi_2O_3 was chosen as the source of bismuth instead of highly soluble $Bi(NO_3)_3$ to avoid unnecessary anion groups which could interfere with the reaction.[73] As for the chalcogen source, the choice is not straightforward. Unlike Na_2S, which is used to provide chalcogen anions in the synthesis of BiAgOS[49], Na_2Se is not an ideal source to provide chalcogen anions in the BiAgOSe synthesis because it is expensive and highly reactive with water. Additionally, selenourea (CH_4N_2Se) or elemental Se under the reductive atmosphere (e.g., hydrazine hydrate) are also not optimal choices for the Se source because they can produce many secondary phases, such as $AgBiSe_2$, Bi_2O_2Se and Ag_2Se, as shown in Figure S1. Therefore, after excluding reagents that are expensive, hazardous or can complicate the reaction, we chose elemental Ag and elemental Se in the BiAgOSe synthesis, where redox reactions between elemental Ag and Se can produce Ag^+ and Se^{2-} ions.

Furthermore, hydrothermal synthesis can be considered as a special case of chemical transport reaction that relies on liquid phase transport of reactants to nucleate the desired product.[74] Therefore, the efficient transport of elements in the solvent is necessary to activate the reaction at such low temperatures.[74,75] Here, the reaction conditions were optimized, including temperature, pH, ratio of reagents and reaction time to dissolve Bi_2O_3, Ag and Se and provide sufficient ions for a high yield of the target phase. For pH, the reagents have a low solubility in water even at the maximum tolerant temperature (513 K) for the Teflon-lined pressure vessel. Therefore, it was needed to add a mineralizer to adjust the reaction pH and increase the solubilities of the reagents. However, acidic mineralizers such as HNO_3, HCl, and H_2SO_4 were avoided because of their propensity to incorporate their own anions into the reaction products. Therefore, NaOH was used as the alkaline mineralizer to guarantee adequate aqueous ions in the reaction. To optimize the suitable amount of mineralizer, reactions with different amounts of NaOH were tested and compared, as shown in Figure S2. With a small amount of NaOH, BiAgOSe forms as a minor product while a large quantity of $AgBiSe_2$ is made. This result indicates that an alkaline environment is necessary for the formation of BiAgOSe. This can be explained by the hydrolysis of Bi_2O_3 in basic solution which provides the indispensable bond between bismuth and oxygen (i.e., $Bi(OH)_4^-$) and suppresses the appearance of homoanionic $AgBiSe_2$.[59] The comparison of driving forces also suggests $Bi(OH)_4^-$ is more likely to be the source ions of bismuth involved in the reaction (see Table S2 reaction 3 and 4). Moreover, as the amount of NaOH increases, the phase fraction of

BiAgOSe increases but unreacted Ag also starts to emerge. Thus, to minimize the number of secondary phases and eliminate $AgBiSe_2$ and Ag simultaneously, 7.5 mmol NaOH was added. With careful mineralizer adjustment, the optimized phase fraction of the target can reach up to ~75% (see Figure S2). To optimize the ratio of reagents, we adjusted the reactant ratios while keeping the amount of NaOH constant at 7.5 mmol as shown in Figure S3. A lower ratio of Ag is helpful to increase the phase fraction of the target phase. However, after adjusting the ratio of reagents, we noticed that unreacted Bi_2O_3, and Bi_2O_2Se and Ag_2Se always exist. To increase the completeness of the reaction and improve the fraction of the target phase, we extended the reaction time with multiple heating profiles as shown in Figure S4 and S5. We found that a longer reaction time is helpful, and the phase fraction of BiAgOSe can be maximized to ~85%.

To further increase the fraction of targeted BiAgOSe phase, it is necessary to eliminate the formation of secondary phases. In general, more than one kind of product are obtained from hydrothermal synthesis owing to several concurrent, highly thermodynamically favorable reactions, and the residue of reagents with low solubilities in water. Therefore, we need to remove side products that could obstruct the production of the target phase. Based on experimental and computational results, we present three likely reactions that progress within our synthetic route to yield BiAgOSe:

$$Bi(OH)_4^- + Ag^+ + Se^{2-} \rightarrow BiAgOSe_{(s)} + 2OH^- + H_2O \quad (1)$$

$$2Bi(OH)_4^- + Se^{2-} \rightarrow Bi_2O_2Se_{(s)} + 4OH^- + 2H_2O \quad (2)$$

$$Bi_2O_2Se_{(s)} + Ag_2Se_{(s)} \rightarrow 2BiAgOSe_{(s)} \quad (3)$$

Our initial synthesis progresses through the competition of reactions (1) and (2), which happen at the same time owing to comparable, highly favorable reaction energies (Table S2). Therefore, the reactions (1) and (2) lead to BiAgOSe accompanied with Bi_2O_2Se. To design a high-yield methodology, Bi_2O_2Se obtained in reaction (2) needs to subsequently react with Ag_2Se to produce BiAgOSe, as in reaction (3). However, the energetic driving force in reaction (3) is quite small (-72.2 meV/f.u., shown in Table S2). Most of the formation energy of the desired quaternary phase in this route is consumed by the formation of the Bi_2O_2Se and Ag_2Se intermediates, which limits the formation of BiAgOSe, as do any energetic barriers to its progression which need to be overcome through seeding (see Figure S6). Therefore, reaction (3) can go to completion when no additional Bi_2O_2Se is produced by reaction (2), necessitating the removal of bismuth oxide and aqueous bismuth ions.

Based on these concepts, we introduce a "subtraction strategy" to assist the formation of the desired product by chemically removing the remaining Bi_2O_3 after the initial reaction period. The synthesis method contains three steps: in the first step, reagents Ag, Se, and Bi_2O_3 are charged in the autoclave. Reactions (1) and (2) take place, for which the target phase BiAgOSe is generated alongside the undesired phases Bi_2O_2Se, Ag_2Se and remaining Bi_2O_3. Then, in the second step, to stop the production of Bi_2O_2Se, we terminate reaction (2) by removing aqueous bismuth ions and unreacted Bi_2O_3 through filtering the solid products and leaching them with 1 M HCl for 2 hours. Finally, in the third step, we hydrothermally react the leached solid product which contains BiAgOSe, Bi_2O_2Se and Ag_2Se. Reaction (3) proceeds with the BiAgOSe seeds produced from reaction (1). The target material as a single phase can be obtained with the three-step method. Figure 2 displays the PXRD of the product after each step, and the SEM images illustrate their morphology. The BiAgOSe crystals show clear facets and the crystallite size ranges from 2 μm to 10 μm.

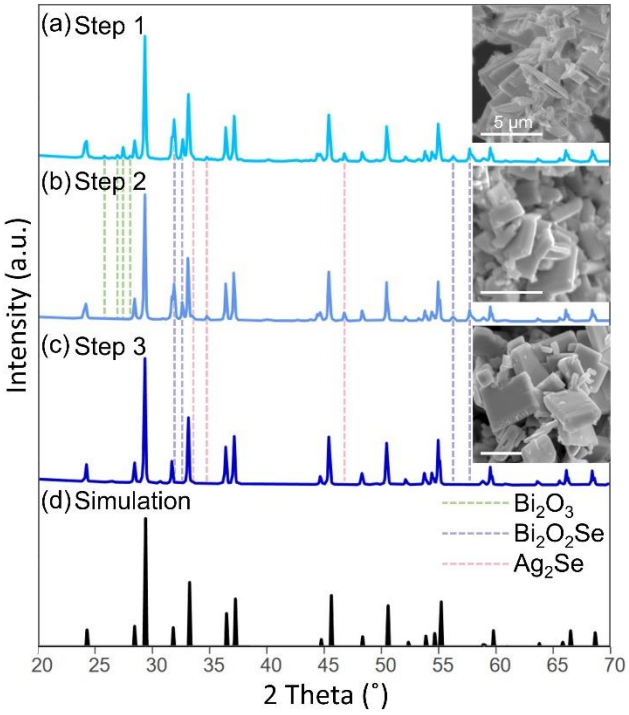

Figure 2. PXRD of products at different synthesis stages. (a) Initial hydrothermal synthesis (Step 1), BiAgOSe, Bi_2O_2Se, Ag_2Se and unreacted Bi_2O_3 are present. (b) Products after removing Bi_2O_3 with 1M HCl for 2 hours (Step 2). (c) Final product (Step 3), where only pure BiAgOSe is present. Insets are SEM (SE) images of products at each stage. (d) Simulated PXRD of BiAgOSe.

Structural Anisotropy Characterization

To determine the crystal structure of the hydrothermally synthesized BiAgOSe powders, Rietveld refinement was performed on the synchrotron diffraction pattern. We confirmed that BiAgOSe is isostructural to BiCuOSe (see Figure 1), which belongs to the *P4/nmm* space group. The unit cells extracted from this refinement are listed in Table S3. Compared to BiCuOSe (JCPDS 45-0296, a = 3.9287(1) Å, c = 8.9291(2) Å), BiAgOSe has larger lattice parameters, which results from the larger ionic radius of Ag^+ (102 pm) than that of Cu^+ (60 pm).[76] The increase of the unit cell resulting from the substitution of Cu by Ag was also observed in BiAgOS and BiCuOS compounds.[49] The tetragonal c/a ratio is 2.36 versus 2.27 in BiAgOSe versus BiCuOSe compounds. BiAgOSe consists of $[Bi_2O_2]^{2+}$ and $[Ag_2Se_2]^{2-}$ layers (sublattices), which are formed by the edge-sharing distorted OBi_4 and $AgSe_4$ tetrahedra, respectively. The positively charged $[Bi_2O_2]^{2+}$ layer and negatively charged $[Ag_2Se_2]^{2-}$ layer are stacked perpendicularly to the c-axis, and interact via electrostatic Coulomb interactions, which makes it different from van der Waals layered materials.

Table S4 indicates that by the substitution of Cu by Ag in the 2*a* Wyckoff position, the M–Se bond is lengthened remarkably (~10%), whereas the bond lengths of Bi–O are rigid and affected only negligibly (< 0.9 %). Since the longer Ag–Se bond length requires larger in-plane space, which is limited by the $[Bi_2O_2]^{2+}$ layer, a larger distortion of $AgSe_4$ tetrahedra than $CuSe_4$ tetrahedra is expected. Indeed, because the bond angles α_1 and α_2 (see Figure 1) of Se–Ag–Se are more deviate from ideal 109.5° than that of Se–Cu–Se (Table S4), the four-coordinate geometry index (τ_4)[77] of $AgSe_4$ versus $CuSe_4$ tetrahedra is 0.87 versus 0.95, which confirms $AgSe_4$ tetrahedra are more distorted than $CuSe_4$ tetrahedra. To understand the origin of this distortion, we perform DFT calculations and apply biaxial strains to the BiAgOSe compound by fixing the two in-plane *a*=*b* lattice constants, and optimizing all atom positions and the *c* lattice parameter. As shown in Figure S7, large in-plane lattice constants lead to less distorted $AgSe_4$ tetrahedra (i.e., smaller difference between α_1 and α_2) and shorter Ag–Se bond lengths. Therefore, the large $AgSe_4$ distortion can be considered as the result from the compromise of the large size mismatch between $[Bi_2O_2]^{2+}$ and $[Ag_2Se_2]^{2-}$ layers of ideal homoleptic tetrahedra. In other words, the $[Ag_2Se_2]^{2-}$ layer is under compressive strain from $[Bi_2O_2]^{2+}$, and $[Bi_2O_2]^{2+}$ is under tensile strain from the $[Ag_2Se_2]^{2-}$ layer because of the smaller size of ideal OBi_4 than $AgSe_4$ tetrahedra. This local distortion affects the lattice thermal conductivity through changing $AgSe_4$ tetrahedra distortion and, therefore, the *d*-*p* orbital hybridization, which affects bond stiffness, sound velocity, and the low-lying phonon eigen displacements. This will be discussed in more detail in the next sections.

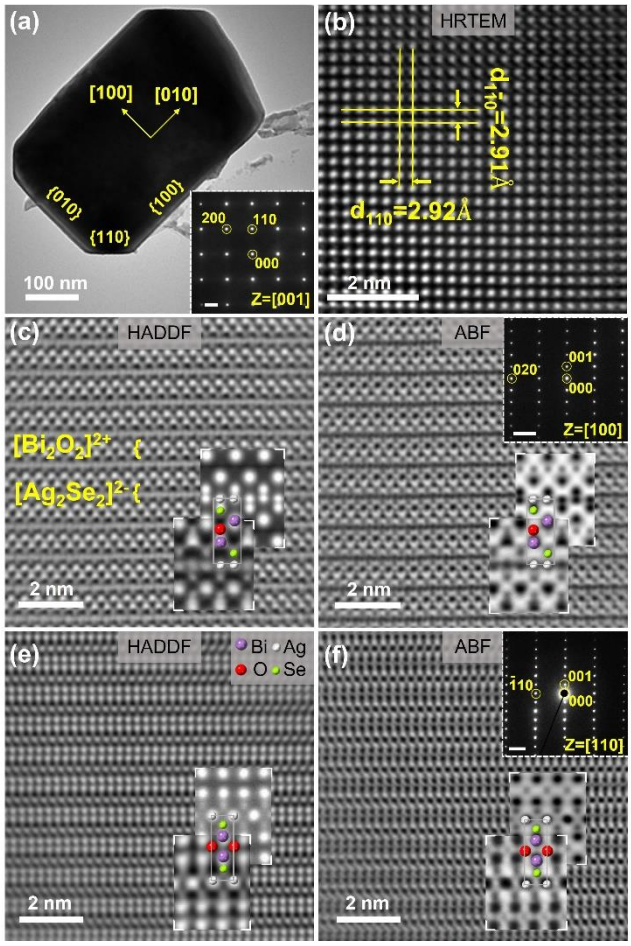

Figure 3. (a) Low magnification conventional TEM image of a faceted BiAgOSe particle produced using the three-step hydrothermal method along the [001] zone axis. The indices of reflections of the SAED pattern inserted in (a) are based on the structure produced from its Rietveld refinement. (b) HRTEM image of the particle along the [001] zone axis. Some lattice planes and their corresponding distances are marked in (b). The index shows that the crystal is terminated with the {100} and {110} surfaces. High-resolution (c) and (e) HAADF and (d) and (f) ABF images along the [100] and [110] zone axes. The overall layered structure can be observed. All the experiment images can match the simulated results and the structure schematics. The scale bars of SAED patterns are 2 nm^{-1}.

Scanning/transmission electron microscopy (S/TEM) analyses were carried out to further investigate the crystal structure of BiAgOSe. Figure 3a is a typical low-magnification TEM image of the hydrothermally synthesized BiAgOSe sample with a faceted shape. The corresponding selected area electron diffraction (SAED) pattern matches well with the refined structure (space group $P4/nmm$) along the [001] zone axis; extra spots, spot splitting, or streaks are not observed. It can be further confirmed that the well-faceted particles obtained from the three-step hydrothermal reaction are terminated with {100} and {110} surfaces, as marked in Figure 3a. Figure 3b displays an HRTEM image of this particle, where the measured interplanar *d*-spacings are in good agreement with the refinement results. Furthermore, simultaneously acquired high angle annular dark field (HAADF) HRSTEM (Figure 3c and e) and annular brightfield (ABF) HRSTEM images (Figure 3d and f) taken along the [100] and [110] zone axes allow direct observation of atomic columns. The SAED patterns of [100] and [110] zone axes inserted in Figure 3d and 3f also match very well with the simulated diffraction pattern (Figure S12). Since the contrast in HAADF depends on the atomic number, the atomic column of Bi (the brightest white dots) and Ag (the second brightest white dots) are distinguishable. To identify the positions of lighter atoms with relatively weaker scattering such as oxygen and selenium, ABF phase-contrast imaging based on wave interference is preferred (Figure 3d and 3f). The inserted higher magnified images (lower) overlaid with simulated STEM images (upper) and structural model shows the clear display of each element. $[Bi_2O_2]^{2+}$ and $[Ag_2Se_2]^{2-}$ layers stacking along the *c*-direction are visible. Chemical analysis with energy-dispersive spectroscopy (EDS) mappings shown in Figure S13 was used to confirm the uniform elemental distribution of Bi, Ag, O and Se in crystals.

Electronic Structure

The DFT calculated band structures of BiAgOSe and BiCuOSe using the PBEsol functional are shown in Figure 4. The band structure of BiAgOSe is very similar to that of BiCuOSe. Both compounds are indirect band semiconductors with small bandgaps (0.24 and 0.14 eV for BiAgOSe and BiCuOSe, respectively) and have multiple bands at the top of the valence bands. The calculated bandgaps using PBEsol are smaller than the experimental measurements (0.96 and 0.80 eV for BiAgOSe and BiCuOSe[46], respectively, see Figure S14) owing to the intrinsic limitation of the semilocal functionals.[78] The main difference between these two band structures is the energy differences (ΔE_v) of the second (Z point) and third (between Z and R) valleys with respect to the VBM (between M

and Γ) in the valence band. BiAgOSe (ΔE_v =124 and 132 meV) has larger energy differences than that of BiCuOSe (ΔE_v = 26 and 70 meV). Therefore, excessive hole doping is required to access the multiband effect in BiAgOSe. The projected electronic density of states (PDOS) shows that the conduction band has Bi 6*p* orbital character, and these orbitals give rise to the highly dispersive conduction band minimum. The larger bandgap of BiAgOSe is due to a weaker Se-4*p* and Ag-4*d* hybridization and the lower Ag–Se antibonding states *p*-*d** formed by Ag-4*d* and Se-4*p* below the Fermi level, which can be seen clearly from the crystal orbital Hamilton population analysis (COHP)[79] in Figure 4. However, the *p*-*d** states of BiAgOSe has larger hybridization with Bi 6*p* than that of BiCuOSe, leading to a larger splitting between the antibonding states and Bi 6*p* states. The weaker coupling between Ag-4*d* and Se-4*p* can also be viewed from the PDOS. The overlap between Ag-4*d* and Se-4*p* orbitals is much smaller than that of Cu-3*d* and Se-4*p* because Ag-4*d* orbitals are too low to hybridize with Se-4*p*. Bader charge calculation shows that there is a larger charge transfer from Cu (Δq_{Cu} = -0.313 *e*) to Se (Δq_{Se} = 0.784 *e*) in BiCuOSe than Ag (Δq_{Ag} = -0.159 *e*) to Se (Δq_{Se} = 0.641 *e*) in BiAgOSe, consistent with the smaller difference in the electronegativities of Ag and Se. Moreover, $AgSe_4$ distortion has large effects on the electronic structures as well. In Figure S8, we show the evolution of the band structure of BiAgOSe as a function of the in-plane lattice constants (or $AgSe_4$ distortion, since α_1 and α_2 are linear increasing and decreasing with lattice constants expanding, see Figure S7). Both the energy difference between the VBM and the second/third peak and the bandgap decrease with the lattice constants increasing (or $AgSe_4$ distortion declining). Therefore, the $AgSe_4$ distortion induced by sublattice mismatch contributes to the large energy difference between valleys close to the Fermi level and large bandgap of BiAgOSe as well. The overlap between Ag-4*d* and Se-4*p* orbitals increases when the distortion of $AgSe_4$ decreasing, as we can see from the antibonding region just below the Fermi level in the COHP plot and the ICOHP (integrated COHP up to the Fermi level) value from Figure S9.

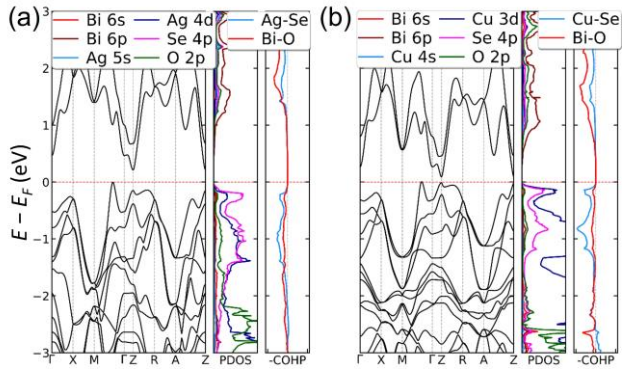

Figure 4. DFT band structures, PDOS, and COHP of (a) BiAgOSe and (b) BiCuOSe calculated using the PBEsol functional including spin-orbit coupling.

Thermal stability and ultralow thermal conductivity

We first investigated the thermal stability of BiAgOSe by variable temperature PXRD under static vacuum (see Figure S15) and found that it is stable up to 673K and it eventually decomposes to Bi_2O_2Se and Ag_2Se at higher temperatures. The differential thermogravimetric analysis (DTA) in Figure S16 shows that the decomposition is endothermic, but the peak is not obvious owing to the small energy difference, which is consistent with the low formation driving force of BiAgOSe from the binary and ternary intermediates (Table S2 reaction 2). Considering its thermal stability and the small size of hydrothermally synthesized particles, BiAgOSe pellets (Figure S11) were spark plasma sintered in argon atmosphere at 573 K for 6 min followed by the second round of SPS at 648 K for 6 min to avoid overheating. The measured total thermal conductivity (κ_{tot}) of BiAgOSe is shown in Figure 5a. The data was measured during heating (red) and cooling (blue) processes. The decent overlap of the heating and cooling curves shows excellent stability of the samples up to 650 K. The total thermal conductivity of BiAgOSe at room temperature is ~0.61 $W{\cdot}m^{-1}{\cdot}K^{-1}$ and decreases to 0.35 $W{\cdot}m^{-1}{\cdot}K^{-1}$ at 650 K. As a contrast, according to previous studies, the total thermal conductivity of the BiCuOSe is generally a higher value, i.e. ~0.62–1.28 $W{\cdot}m^{-1}{\cdot}K^{-1}$ at room temperature and declines to ~0.45–0.76 $W{\cdot}m^{-1}{\cdot}K^{-1}$ at 650 K.[28–34] One example from Reference 34 is plotted in Figure 5a as comparison. Note that lattice thermal conductivity κ_L is assumed to approach κ_{tot} because of the negligible electronic contribution (κ_{ele}) in the intrinsic sample. Figure 5b displays the calculated κ_L for BiAgOSe along the *a* ($\kappa_L^{\perp}$) and *c* ($\kappa_L^{\parallel}$) axes, and the average lattice thermal conductivity ($\overline{\kappa_L}$) at various temperatures. Although the calculated κ_L is slightly higher than the experimental value, the overall trend agrees with the experiment. The overestimation of κ_L is likely because lattice thermal expansion and other phonon–phonon scattering mechanisms such as four phonon scattering[80], defects, and grain boundary are not included in the current calculations.

Origin of ultralow thermal conductivity

To understand the microscopic mechanism behind the low κ_L of BiAgOSe, we performed lattice dynamical calculations based on DFT-PBEsol calculated force constants. The phonon dispersions and density of states (DOS) are shown in Figure 5c. As previously mentioned, the compound is a superlattice structure with alternating $[Bi_2O_2]^{2+}$ and $[Ag_2Se_2]^{2-}$ layers. Therefore, the frequency of the highest acoustic phonon mode (longitudinal acoustic, LA) along the Γ-Z (stacking) direction is only ~50 cm^{-1}, due to the weak interlayer interactions. A remarkable character of the phonon dispersion is the low-frequency phonon modes along Γ-M and A-Z lines, which leads to very low phonon velocities of the transverse acoustic (TA) modes within the layer. Overall, the phonon frequencies of the compound are quite low.

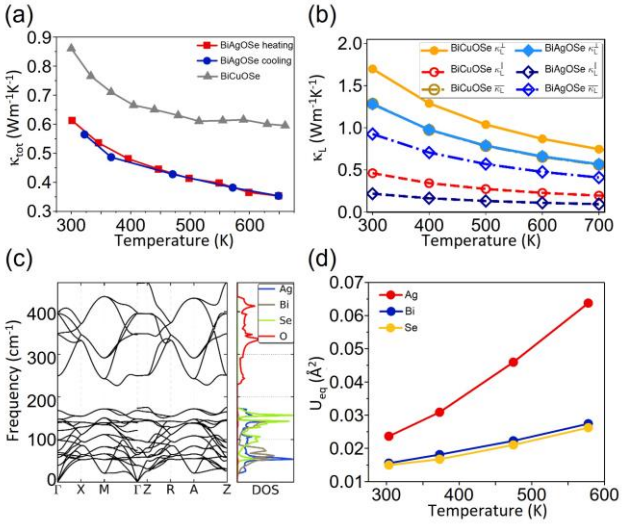

Figure 5. (a) Temperature-dependent total thermal conductivity of BiAgOSe during heating (red) and cooling (blue) process; the total thermal conductivity of BiCuOSe (gray) from reference[34] is included as comparison. (b) DFT calculated lattice thermal conductivity along a ($\kappa_L^{\perp}$) and c ($\kappa_L^{\parallel}$) crystallographic directions and average ($\bar{\kappa}$) lattice thermal conductivity of BiAgOSe and BiCuOSe. (c) Phonon dispersion curves and density of states (DOS) of BiAgOSe. The longitudinal optical-transverse optical (LO-TO) splitting is included. (d) Experimental ADPs of BiAgOSe as a function of temperature.

As we can see from the phonon DOS in Figure 5c, the low-lying peaks are mainly from Bi and Ag. The phonon frequency is inversely proportional to the square root of reduced mass and proportional to the square root of force constants (bond stiffness). The low-frequency modes associated with Bi are expected because of its heavy reduced mass. The low frequency associated with Ag is due to the flexible Ag–Se bond, as evident from our calculation that the interatomic force constants (the absolute value sum of all the force constant matrix elements) between Ag and Se in BiAgOSe (3.3 eV/Å^2) are smaller than that between Cu and Se in BiCuOSe (4.2 eV/Å^2). The sharp peak of Ag at ~50 cm^{-1} corresponds to the flat bands crossing the whole Brillouin zone, which indicates very localized atom vibrations. The intensity of the Ag peak is much higher than that of Se at the same energy region. This suggests that the Ag displacements are largely decoupled from the ligand (Se) displacements. Therefore, these flat bands are mainly due to the localized vibrations of Ag atoms, as evidenced from the real space displacements of the phonon modes at the selected high symmetry points in Figure S10. To further support this conclusion from experiment, we then measured the temperature dependent atomic displacement parameters (ADP) to characterize the mean square displacement of an atom from its equilibrium position, as shown in Figure 5d. ADP (listed in Table S5) increases almost linearly with temperature; and Ag has the largest ADP and the fastest increasing rate, which indicates its large vibration.

Table 1. Einstein (Θ_E) of M (M=Ag, Cu) and Debye (Θ_D) temperatures of Bi and Se atoms, the frequency of the localized M mode (ν_M) determined from analysis of synchrotron diffraction data, and Debye temperature and average velocity of sound (υ_s) of BiAgOSe and BiCuOSe estimated from the specific heat capacity.

Materials	Θ_E (M) /K	ν_M /cm^{-1}	Θ_D (Bi) /K	Θ_D (Se) /K	Θ_D /K	υ_s /m·s^{-1}
BiAgOSe	55	38	127	210	191	1873
BiCuOSe	116	80	133	271	219	2085

To compare the thermal transport properties of BiAgOSe and BiCuOSe in more detail, we estimated their Debye temperatures and sound velocities from the synchrotron data. A typical fit is shown in Figure S18. Ag atom is treated as an individual quantum harmonic oscillator (Einstein Oscillators) because of its considerably large ADP (more than 2.5 times of other atoms).[81] Therefore, Ag is considered within the Einstein model, while the other atoms are treated as Debye hosts. Thus, the Einstein temperature for Ag atom can be determined from the slope of its ADP versus temperature, as tabulated in Table 1. The estimated Einstein temperature corresponds to a frequency of 38 cm^{-1}, which is close to the calculated peak of Ag in our DOS at ~50 cm^{-1}. In this vein, Debye temperatures of Bi and Se can be extracted from ADP data by considering them as stiff frameworks. The corresponding values of BiCuOSe were also estimated from synchrotron data (Figure S19) using the above method. Although compared to the previous study of BiCuOSe[38], the estimations from X-ray diffraction are higher than that of neutron diffraction, which is caused by the nature of different diffraction sources[62], the ADPs show the same trend. Both Ag and Cu show extreme low Θ_E, which is even comparable to rattler atoms in many low thermal conductive compounds with cage structure[61,62]. The overall Debye temperatures and the average sound velocity of BiAgOSe and BiCuOSe were estimated from the specific heat capacity at 2.6–3.5 K (Figure S17), as shown in Table 1. The estimated Debye temperature for BiCuOSe agrees with the literature data (210 K estimated from neutron diffraction[38] and 245 K estimated from heat capacity[82]). A lower Debye temperature and sound velocity of BiAgOSe than BiCuOSe leads to a lower thermal conductivity, which is mainly contributed by Ag because of its lower Einstein temperature and lower frequency of the vibration mode.

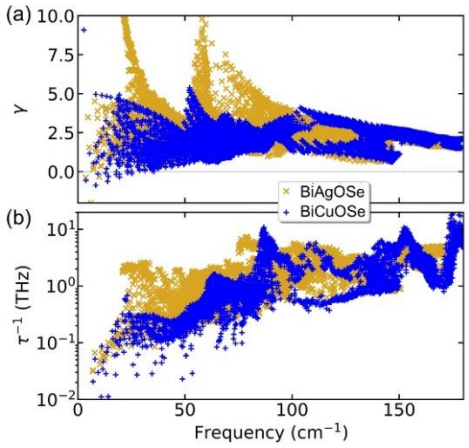

Figure 6. DFT calculated (a) Grüneisen parameters γ and (b) phonon–phonon scattering rate τ^{-1} of BiAgOSe and BiCuOSe.

Because the increase of APD of Ag atoms is faster at higher temperatures, there is deviation between the linear fitting and the experimental data. The deviation is associated with the anharmonic motion of Ag, which should be further considered. Therefore, we compare the Grüneisen parameters (γ), which reflects bond anharmonicity,[83] and three phonon–phonon scattering rate (τ^{-1}), which is the inverse of phonon relaxation time (τ) of these two compounds. The calculated γ and τ^{-1} are shown in Figure 6a and b, respectively. BiAgOSe has larger γ and higher τ^{-1} than BiCuOSe in the low-frequency (< 100 cm^{-1}) region, where phonons carry most of the heat. The strong phonon–phonon scattering within this frequency region effectively lowers the phonon relaxation time and subsequently reduces κ_L in BiAgOSe. In Figure 6a, there are two main peaks of γ. According to their corresponding frequencies and the DOS of Figure 5c and S10, we can see that the peak of γ at ~60 cm^{-1} is mainly due to Bi and Ag, and the peak at ~25 cm^{-1} is mainly due to Ag atoms. The contribution from Bi is attributed to the lone-pair electrons,[84] while the contribution of Ag is larger and at even lower frequency regions, which primarily originates from the flexible bonds (Ag–Se). Except for the relatively weak antibonding interaction between Ag and Se, as mentioned above, the large sublattice mismatch between $[Bi_2O_2]^{2+}$ and $[Ag_2Se_2]^{2-}$ layers in BiAgOSe results in more distorted $AgSe_4$ than $CuSe_4$ tetrahedra. The large deviation from the ideal tetrahedra ($\alpha_1=\alpha_2=109.5°$) reduces the orbital overlap/coupling between Ag-4*d* and Se-4*p* orbitals, which results in a lower Ag–Se bond stiffness and more localized Ag displacement (rattling-like behavior). Therefore, the mismatch between $[Bi_2O_2]^{2+}$ and $[Ag_2Se_2]^{2-}$ layers in the layered mixed anion compound with homoleptic coordination can tune phonon interactions as well, which provides an extra avenue for engineering a material's phonon transport properties.

In summary, the low lattice thermal conductivity of BiAgOSe arises from both low speed of sound and short phonon relaxation time. The antibonding interaction originating from the unusual hybridization between Ag-4*d* and Se-4*p* together with large sublattice mismatch between $[Bi_2O_2]^{2+}$ and $[Ag_2Se_2]^{2-}$ layers lead to low stiff Ag–Se bonds, large distorted $AgSe_4$ tetrahedra and less rigid $[Ag_2Se_2]^{2-}$ layers, which results in small phonon velocities within the layer. The strong phonon–phonon scattering originating from the localized Ag atoms further reduces the thermal conductivity.

Conclusion

In this work, we describe the hydrothermal synthesis of pure BiAgOSe. This was accomplished via the "subtraction strategy", which has been developed to overcome the difficulty of forming BiAgOSe from the binary and ternary intermediates, whose high stability typically prevents the reaction. Specifically, through chemically removing unreacted Bi_2O_3, we have suppressed the formation of the stable Bi_2O_2Se intermediate, which consumes most of the formation energy necessary to synthesize BiAgOSe. Both refined PXRD and TEM reveal that the as-made BiAgOSe is isostructural to BiCuOSe, and contains $[Bi_2O_2]^{2+}$ and $[Ag_2Se_2]^{2-}$ layers stacking perpendicularly to the *c*-axis. BiAgOSe has a larger sublattice mismatch between layers owing to the larger ionic radius of Ag than Cu. Electronic structure studies show that BiAgOSe is an indirect bandgap semiconductor with bandgap of 0.95 eV, which is larger than that of BiCuOSe. This is due to the weaker hybridization between Ag-4*d* and Se-4*p* than that between Cu-3*d* and Se-4*p*. More importantly, BiAgOSe exhibits a lower thermal conductivity (~0.61 $W{\cdot}m^{-1}{\cdot}K^{-1}$ at room temperature and ~0.35 $W{\cdot}m^{-1}{\cdot}K^{-1}$ at 650 K) than BiCuOSe, which is one of the best thermoelectric materials at moderate temperatures. The combination of DFT calculations and X-ray diffraction experiments reveals that the low thermal transport behavior comes from both slow sound velocities and strong lattice anharmonicity. ADP measurements along with lattice dynamic calculations demonstrate that the Ag atom, owing to the less stiff Ag–Se bond, has the largest contribution to the strong anharmonicity and high phonon–phonon scattering rates. Our results show that BiAgOSe is a promising material for low thermal conductivity applications, particularly for high-performance thermoelectric materials. The sublattice mismatch between layers formed by different homoleptic polyhedra in layered heteroanionic compounds can be used as an extra degree of freedom to engineer electronic structures and phonon transport properties of new materials.

ASSOCIATED CONTENT

Supporting Information

Crystallographic data (CIF)

CCDC 2111345 contains the supplementary crystallographic data for this paper. These data can be obtained free of charge via www.ccdc.cam.ac.uk/data_request/cif, or by emailing data_request@ccdc.cam.ac.uk, or by contacting The Cambridge Crystallographic Data Centre, 12 Union Road, Cambridge CB2 1EZ, UK; fax: +44 1223 336033.

PXRD patterns of products under different reaction conditions, additional DFT calculation details, S/TEM images and EDS, diffuse reflectance curves, DTA curves, heat capacity data, results of the Rietveld refinement, additional crystallographic details.

AUTHOR INFORMATION

Corresponding Author

Kenneth R. Poeppelmeier: krp@northwestern.edu
Vinayak P. Dravid: v-dravid@northwestern.edu

Notes

The authors declare no competing financial interest.

ACKNOWLEDGMENT

We thank MRSEC program (NSF DMR-1720139) at the Materials Research Center of Northwestern University for funding. This work made use of the Advanced Photon Source at Argonne National Laboratory (ANL) (supported by the U.S. Department of Energy, Office of Science, Office of Basic Energy Sciences, under Contract No. DE-AC02-06CH11357) with the help from Dr. Saul Lapidus, the facility for heat capacity measurements at ANL supported by the U.S. Department of Energy, Office of Science, Basic Energy Sciences, Materials Science and Engineering Division, the facility of KeckBio in Northwestern University with the assistance from Ms. Eleanor Dunietz, Northwestern's IMSERC Crystallography facility and the Jerome B. Cohen X-Ray Diffraction Facility. This work also

made use of EPIC facility of Northwestern University's NU*ANCE* Center, which has received support from the Soft and Hybrid Nanotechnology Experimental (SHyNE) Resource (NSF ECCS-2025633), the MRSEC program (DMR-1720139), the International Institute for Nanotechnology (IIN), the Keck Foundation, and the State of Illinois. The authors acknowledge the computing resources provided by the National Energy Research Scientific Computing Center (NERSC), a U.S. Department of Energy Office of Science User Facility operated under Contract No. DE-AC02-05CH11231, the Extreme Science and Engineering Discovery Environment (National Science Foundation Contract ACI-1548562), and the Quest high performance computing facility at Northwestern University. We also thank the Department of Energy, Office of Science, Basic Energy Sciences under grant DE-SC0014520 for thermal property measurements.

REFERENCES

(1) Antusch, S.; Reiser, J.; Hoffmann, J.; Onea, A. Refractory Materials for Energy Applications. *Energy Technol.* **2017**, *5*, 1064–1070.
(2) Wu, J.; Wei, X.; Padture, N. P.; Klemens, P. G.; Gell, M.; García, E.; Miranzo, P.; Osendi, M. I. Low-Thermal-Conductivity Rare-Earth Zirconates for Potential Thermal-Barrier-Coating Applications. *J. Am. Ceram. Soc.* **2002**, *85*, 3031–3035.
(3) Darolia, R. Thermal Barrier Coatings Technology: Critical Review, Progress Update, Remaining Challenges and Prospects. *Int. Mater. Rev.* **2013**, *58*, 315–348.
(4) Matsunaga, T.; Yamada, N.; Kojima, R.; Shamoto, S.; Sato, M.; Tanida, H.; Uruga, T.; Kohara, S.; Takata, M.; Zalden, P.; Bruns, G.; Sergueev, I.; Wille, H. C.; Hermann, R. P.; Wuttig, M. Phase-Change Materials: Vibrational Softening upon Crystallization and Its Impact on Thermal Properties. *Adv. Funct. Mater.* **2011**, *21*, 2232–2239.
(5) DiSalvo, F. J. Thermoelectric Cooling and Power Generation. *Science* **1999**, *285*, 703–706.
(6) Rowe, D. M. (Ed.) *CRC Handbook of Thermoelectrics*; CRC Press: Boca Raton, FL, 1995.
(7) Snyder, G. J.; Toberer, E. S. Complex Thermoelectric Materials. In *Materials for Sustainable Energy*; Co-Published with Macmillan Publishers Ltd, UK, 2010; pp 101–110.
(8) He, J.; Kanatzidis, M. G.; Dravid, V. P. High Performance Bulk Thermoelectrics via a Panoscopic Approach. *Mater. Today.* **2013**, *16*, 166–176.
(9) Zeier, W. G.; Zevalkink, A.; Gibbs, Z. M.; Hautier, G.; Kanatzidis, M. G.; Snyder, G. J. Thinking Like a Chemist: Intuition in Thermoelectric Materials. *Angew. Chem. Int. Ed.* **2016**, 55, 6826–6841.
(10) Tan, G.; Zhao, L.-D.; Kanatzidis, M. G. Rationally Designing High-Performance Bulk Thermoelectric Materials. *Chem. Rev.* **2016**, *116*, 12123–12149.
(11) Pal, K.; Xia, Y.; He, J.; Wolverton, C. Intrinsically Low Lattice Thermal Conductivity Derived from Rattler Cations in an AMM′ Q_3 Family of Chalcogenides. *Chem. Mater.* **2019**, *31*, 8734–8741.
(12) Chen, Z.-G.; Shi, X.; Zhao, L.-D.; Zou, J. High-Performance SnSe Thermoelectric Materials: Progress and Future Challenge. *Prog. Mater. Sci.* **2018**, *97*, 283–346.
(13) Luo, Z.-Z.; Cai, S.; Hao, S.; Bailey, T. P.; Hu, X.; Hanus, R.; Ma, R.; Tan, G.; Chica, D. G.; Snyder, G. J.; Uher, C.; Wolverton, C.; Dravid, V. P.; Yan, Q.; Kanatzidis, M. G. Ultralow Thermal Conductivity and High-Temperature Thermoelectric Performance in n-Type $K_{2.5}Bi_{8.5}Se_{14}$. *Chem. Mater.* **2019**, *31*, 5943–5952.
(14) Cai, S.; Hao, S.; Luo, Y.; Su, X.; Luo, Z.-Z.; Hu, X.; Wolverton, C.; Dravid, V. P.; Kanatzidis, M. G. Ultralow Thermal Conductivity and Thermoelectric Properties of $Rb_2Bi_8Se_{13}$. *Chem. Mater.* **2020**, *32*, 3561–3569.
(15) Lin, H.; Tan, G.; Shen, J.-N.; Hao, S.; Wu, L.-M.; Calta, N.; Malliakas, C.; Wang, S.; Uher, C.; Wolverton, C.; Kanatzidis, M. G. Concerted Rattling in $CsAg_5Te_3$ Leading to Ultralow Thermal Conductivity and High Thermoelectric Performance. *Angew. Chem.* **2016**, *128*, 11603–11608.
(16) Tan, G.; Hao, S.; Zhao, J.; Wolverton, C.; Kanatzidis, M. G. High Thermoelectric Performance in Electron-Doped $AgBi_3S_5$ with Ultralow Thermal Conductivity. *J. Am. Chem. Soc.* **2017**, *139*, 6467–6473.
(17) Jia, N.; Cao, J.; Tan, X. Y.; Dong, J.; Liu, H.; Tan, C. K. I.; Xu, J.; Yan, Q.; Loh, X. J.; Suwardi, A. Thermoelectric Materials and Transport Physics. Mater. *Today Phys.* **2021**, *21*, 100519.
(18) Toberer, E. S.; Zevalkink, A.; Snyder, G. J. Phonon Engineering through Crystal Chemistry. *J. Mater. Chem.* **2011**, *21*, 15843–15852.
(19) Clarke, S. J.; Adamson, P.; Herkelrath, S. J. C.; Rutt, O. J.; Parker, D. R.; Pitcher, M. J.; Smura, C. F. Structures, Physical Properties, and Chemistry of Layered Oxychalcogenides and Oxypnictides. *Inorg. Chem.* **2008**, *47*, 8473–8486.
(20) Muir, S.; Subramanian, M. A. ZrCuSiAs Type Layered Oxypnictides: A Bird's Eye View of LnMPnO Compositions. *Prog. Solid. State Chem.* **2012**, *40*, 41–56.
(21) Kageyama, H.; Hayashi, K.; Maeda, K.; Attfield, J. P.; Hiroi, Z.; Rondinelli, J. M.; Poeppelmeier, K. R. Expanding Frontiers in Materials Chemistry and Physics with Multiple Anions. *Nat. Commun.* **2018**, *9*, 1–15.
(22) Harada, J. K.; Charles, N.; Poeppelmeier, K. R.; Rondinelli, J. M. Heteroanionic Materials by Design: Progress Toward Targeted Properties. *Adv. Mater.* **2019**, *31*, 1805295.
(23) Pearson, R. G. Hard and Soft Acids and Bases, HSAB, Part 1: Fundamental Principles. *J. Chem. Educ.* **1968**, *45*, 581.
(24) Zhao, L.-D.; Lo, S.-H.; Zhang, Y.; Sun, H.; Tan, G.; Uher, C.; Wolverton, C.; Dravid, V. P.; Kanatzidis, M. G. Ultralow Thermal Conductivity and High Thermoelectric Figure of Merit in SnSe Crystals. *Nature* **2014**, *508*, 373–377.
(25) Zhao, L.-D.; Tan, G.; Hao, S.; He, J.; Pei, Y.; Chi, H.; Wang, H.; Gong, S.; Xu, H.; Dravid, V. P.; Uher, C.; Snyder, G. J.; Wolverton, C.; Kanatzidis, M. G. Ultrahigh Power Factor and Thermoelectric Performance in Hole-Doped Single-Crystal SnSe. *Science* **2016**, *351*, 141–144.
(26) Chang, C.; Wu, M.; He, D.; Pei, Y.; Wu, C.-F.; Wu, X.; Yu, H.; Zhu, F.; Wang, K.; Chen, Y.; Huang, L.; Li, J.-F.; He, J.; Zhao, L.-D. 3D Charge and 2D Phonon Transports Leading to High Out-of-Plane ZT in n-Type SnSe Crystals. *Science* **2018**, *360*, 778–783.
(27) Gibson, Q. D.; Zhao, T.; Daniels, L. M.; Walker, H. C.; Daou, R.; Hébert, S.; Zanella, M.; Dyer, M. S.; Claridge, J. B.; Slater, B.; Gaultois, M. W.; Corà, F.; Alaria, J.; Rosseinsky, M. J. Low Thermal Conductivity in a Modular Inorganic Material with Bonding Anisotropy and Mismatch. *Science* **2021**, *373*, 1017–1022.
(28) Zhao, L. D.; Berardan, D.; Pei, Y. L.; Byl, C.; Pinsard-Gaudart, L.; Dragoe, N. $Bi_{1-x}Sr_xCuSeO$ Oxyselenides as Promising Thermoelectric Materials. *Appl. Phys. Lett* **2010**, *97*, 092118.
(29) Pei, Y.-L.; He, J.; Li, J.-F.; Li, F.; Liu, Q.; Pan, W.; Barreteau, C.; Berardan, D.; Dragoe, N.; Zhao, L.-D. High Thermoelectric

Performance of Oxyselenides: Intrinsically Low Thermal Conductivity of Ca-Doped BiCuSeO. *NPG Asia Mater.* **2013**, *5*, e47–e47.
(30) Zhao, L.-D.; He, J.; Berardan, D.; Lin, Y.; Li, J.-F.; Nan, C.-W.; Dragoe, N. BiCuSeO Oxyselenides: New Promising Thermoelectric Materials. *Energy Environ. Sci.* **2014**, *7*, 2900–2924.
(31) Ren, G.-K.; Lan, J.; Butt, S.; J. Ventura, K.; Lin, Y.-H.; Nan, C.-W. Enhanced Thermoelectric Properties in Pb-Doped BiCuSeO Oxyselenides Prepared by Ultrafast Synthesis. *RSC Adv.* **2015**, *5*, 69878–69885.
(32) Wen, Q.; Chang, C.; Pan, L.; Li, X.; Yang, T.; Guo, H.; Wang, Z.; Zhang, J.; Xu, F.; Zhang, Z.; Tang, G. Enhanced Thermoelectric Performance of BiCuSeO by Increasing Seebeck Coefficient through Magnetic Ion Incorporation. *J. Mater. Chem. A* **2017**, *5*, 13392–13399.
(33) Das, S.; Valiyaveettil, S. M.; Chen, K.-H.; Suwas, S.; Mallik, R. C. Thermoelectric Properties of Mn Doped BiCuSeO. *Mater. Res. Express* **2019**, *6*, 086305.
(34) Li, Z.; Xiao, C.; Fan, S.; Deng, Y.; Zhang, W.; Ye, B.; Xie, Y. Dual Vacancies: An Effective Strategy Realizing Synergistic Optimization of Thermoelectric Property in BiCuSeO. *J. Am. Chem. Soc.* **2015**, *137*, 6587–6593.
(35) Berdonosov, P.; Kusainova, A.; Kholodkovskaya, L.; Dolgikh, V.; Akselrud, L.; Popovkin, B. Powder X-Ray and IR Studies of the New Oxyselenides MOCuSe (M= Bi, Gd, Dy). *J. Solid State Chem.* **1995**, *118*, 74–77.
(36) Pöttgen, R.; Johrendt, D. Materials with ZrCuSiAs-Type Structure. *Z. Naturforsch. B* **2008**, *63*, 1135–1148.
(37) Barreteau, C.; Berardan, D.; Dragoe, N. Studies on the Thermal Stability of BiCuSeO. *J. Solid State Chem.* **2015**, *222*, 53–59.
(38) Vaqueiro, P.; Al Orabi, R. A. R.; Luu, S. D. N.; Guélou, G.; Powell, A. V.; Smith, R. I.; Song, J.-P.; Wee, D.; Fornari, M. The Role of Copper in the Thermal Conductivity of Thermoelectric Oxychalcogenides: Do Lone Pairs Matter? *Phys. Chem. Chem. Phys.* **2015**, *17*, 31735–31740.
(39) Gamon, J.; Giaume, D.; Wallez, G.; Labégorre, J.-B.; Lebedev, O. I.; Al Rahal Al Orabi, R.; Haller, S.; Le Mercier, T.; Guilmeau, E.; Maignan, A.; Barboux, P. Substituting Copper with Silver in the BiMOCh Layered Compounds (M = Cu or Ag; Ch = S, Se, or Te): Crystal, Electronic Structure, and Optoelectronic Properties. *Chem. Mater.* **2018**, *30*, 549–558.
(40) Li, J.; Zhang, C.; Yan, Y.; Yang, J.; Shi, B.; Wang, Y.; Cheng, Z. Predicting Excellent Anisotropic Thermoelectric Performance of the Layered Oxychalcogenides BiAgOCh (Ch = S, Se, and Te). *Comput. Mater. Sci.* **2020**, *171*, 109273.
(41) He, J.; Yao, Z.; I. Hegde, V.; Naghavi, S. S.; Shen, J.; Bushick, K. M.; Wolverton, C. Computational Discovery of Stable Heteroanionic Oxychalcogenides ABXO (A, B = Metals; X = S, Se, Te) and Their Potential Applications. *Chem. Mater.* **2020**, *32*, 8229-8242.
(42) Farooq, M. U.; Butt, S.; Gao, K.; Pang, X. L.; Sun, X.; Asfandiyar; Mohmed, F.; Ahmad, A.; Mahmood, A.; Mahmood, N. Improved Thermoelectric Performance of BiCuSeO by Ag Substitution at Cu Site. *J. Alloys Compd.* **2017**, *691*, 572–577.
(43) Li, F.; Zheng, Z.; Chang, Y.; Ruan, M.; Ge, Z.; Chen, Y.; Fan, P. Synergetic Tuning of the Electrical and Thermal Transport Properties via Pb/Ag Dual Doping in BiCuSeO. *ACS Appl. Mater. Interfaces* **2019**, *11*, 45737–45745.
(44) Kholodkovskaya, L. N.; Akselrud, L. G.; Kusainova, A. M.; Dolgikh, V. A.; Popovkin, B. A. BiCuSeO: Synthesis and Crystal Structure. *Mater. Sci. Forum* **1993**, *133–136*, 693–696.
(45) Kusainova, A. M.; Berdonosov, P. S.; Akselrud, L. G.; Kholodkovskaya, L. N.; Dolgikh, V. A.; Popovkin, B. A. New Layered Compounds with the General Composition (MO) (CuSe), Where M = Bi, Nd, Gd, Dy, and BiOCuS: Syntheses and Crystal Structure. *J. Solid State Chem.* **1994**, *112*, 189–191.
(46) Hiramatsu, H.; Yanagi, H.; Kamiya, T.; Ueda, K.; Hirano, M.; Hosono, H. Crystal Structures, Optoelectronic Properties, and Electronic Structures of Layered Oxychalcogenides *M*CuO*Ch* (*M* = Bi, La; *Ch* = S, Se, Te): Effects of Electronic Configurations of M^{3+} Ions. *Chem. Mater.* **2008**, *20*, 326–334.
(47) Richard, A. P.; Russell, J. A.; Zakutayev, A.; Zakharov, L. N.; Keszler, D. A.; Tate, J. Synthesis, Structure, and Optical Properties of BiCuOCh (Ch=S, Se, and Te). *J. Solid State Chem.* **2012**, *187*, 15–19.
(48) Chan, G. H.; Deng, B.; Bertoni, M.; Ireland, J. R.; Hersam, M. C.; Mason, T. O.; Van Duyne, R. P.; Ibers, J. A. Syntheses, Structures, Physical Properties, and Theoretical Studies of CeM_xOS (M = Cu, Ag; x ≈ 0.8) and CeAgOS. *Inorg. Chem.* **2006**, *45*, 8264–8272.
(49) BaQais, A.; Curutchet, A.; Ziani, A.; Ait Ahsaine, H.; Sautet, P.; Takanabe, K.; Le Bahers, T. Bismuth Silver Oxysulfide for Photoconversion Applications: Structural and Optoelectronic Properties. *Chem. Mater.* **2017**, *29*, 8679–8689.
(50) McClain, R.; Malliakas, C. D.; Shen, J.; Wolverton, C.; Kanatzidis, M. G. *In Situ* Mechanistic Studies of Two Divergent Synthesis Routes Forming the Heteroanionic BiOCuSe. *J. Am. Chem. Soc.* **2021**, *143*, 12090-12099.
(51) Wustrow, A.; Key, B.; Phillips, P. J.; Sa, N.; Lipton, A. S.; Klie, R. F.; Vaughey, J. T.; Poeppelmeier, K. R. Synthesis and Characterization of $MgCr_2S_4$ Thiospinel as a Potential Magnesium Cathode. *Inorg. Chem.* **2018**, *57*, 8634–8638.
(52) Todd, P. K.; McDermott, M. J.; Rom, C. L.; Corrao, A. A.; Denney, J. J.; Dwaraknath, S. S.; Khalifah, P. G.; Persson, K. A.; Neilson, J. R. Selectivity in Yttrium Manganese Oxide Synthesis via Local Chemical Potentials in Hyperdimensional Phase Space. *J. Am. Chem. Soc.* **2021**, *143*, 15185–15194.
(53) Gopalakrishnan, J. Chimie Douce Approaches to the Synthesis of Metastable Oxide Materials. *Chem. Mater.* **1995**, *7*, 1265–1275.
(54) Dawson, W. J. Hydrothermal Synthesis of Advanced Ceramic Powders. *Am. Ceram. Soc. bull* **1988**, *67*, 1673–1678.
(55) Yoshimura, M. Importance of Soft Solution Processing for Advanced Inorganic Materials. *J. Mater. Res.* **1998**, *13*, 796–802.
(56) Yu, S.-H. Hydrothermal/Solvothermal Processing of Advanced Ceramic Materials. *J. Ceram. Soc. Jpn.* **2001**, *109*, S65–S75.
(57) Sheets, W. C.; Stampler, E. S.; Kabbour, H.; Bertoni, M. I.; Cario, L.; Mason, T. O.; Marks, T. J.; Poeppelmeier, K. R. Facile Synthesis of BiCuOS by Hydrothermal Methods. *Inorg. Chem.* **2007**, *46*, 10741–10748.
(58) Stampler, E. S.; Sheets, W. C.; Bertoni, M. I.; Prellier, W.; Mason, T. O.; Poeppelmeier, K. R. Temperature Driven Reactant Solubilization Synthesis of BiCuOSe. *Inorg. Chem.* **2008**, *47*, 10009–10016.
(59) Walters, L. N.; Zhang, C.; Dravid, V. P.; Poeppelmeier, K. R.; Rondinelli, J. M. First-Principles Hydrothermal Synthesis Design to Optimize Conditions and Increase the Yield of Quaternary Heteroanionic Oxychalcogenides. *Chem. Mater.* **2021**, *33*, 2726–2741.
(60) Toby, B. H.; Von Dreele, R. B. GSAS-II: The Genesis of a Modern Open-Source All Purpose Crystallography Software Package. *J. Appl. Crystallogr.* **2013**, *46*, 544–549.

(61) Sales, B. C.; Chakoumakos, B. C.; Mandrus, D.; Sharp, J. W. Atomic Displacement Parameters and the Lattice Thermal Conductivity of Clathrate-like Thermoelectric Compounds. *J. Solid State Chem.* **1999**, *146*, 528–532.
(62) Sales, B. C.; Mandrus, D. G.; Chakoumakos, B. C. Chapter 1 Use of Atomic Displacement Parameters in Thermoelectric Materials Research. In *Semiconductors and Semimetals*; Elsevier, 2001; Vol. 70, pp 1–36.
(63) Kresse, G.; Furthmüller, J. Efficiency of Ab-Initio Total Energy Calculations for Metals and Semiconductors Using a Plane-Wave Basis Set. *Comput. Mater. Sci.* **1996**, *6*, 15–50.
(64) Kresse, G.; Furthmüller, J. Efficient Iterative Schemes for Ab Initio Total-Energy Calculations Using a Plane-Wave Basis Set. *Phys. Rev. B* **1996**, *54*, 11169–11186
(65) Perdew, J. P.; Ruzsinszky, A.; Csonka, G. I.; Vydrov, O. A.; Scuseria, G. E.; Constantin, L. A.; Zhou, X.; Burke, K. Restoring the Density-Gradient Expansion for Exchange in Solids and Surfaces. *Phys. Rev. Lett.* **2008**, *100*, 136406.
(66) Blöchl, P. E. Projector Augmented-Wave Method. *Phys. Rev. B* **1994**, *50*, 17953–17979.
(67) Ahuja, R.; Blomqvist, A.; Larsson, P.; Pyykkö, P.; Zaleski-Ejgierd, P. Relativity and the Lead-Acid Battery. *Phys. Rev. Lett.* **2011**, *106*, 018301.
(68) Deringer, V. L.; Tchougréeff, A. L.; Dronskowski, R. Crystal Orbital Hamilton Population (COHP) Analysis As Projected from Plane-Wave Basis Sets. *J. Phys. Chem. A* **2011**, *115*, 5461–5466.
(69) Togo, A.; Tanaka, I. First Principles Phonon Calculations in Materials Science. *Scr. Mater.* **2015**, *108*, 1–5.
(70) Li, W.; Lindsay, L.; Broido, D. A.; Stewart, D. A.; Mingo, N. Thermal Conductivity of Bulk and Nanowire $Mg_2Si_xSn_{1-x}$ Alloys from First Principles. *Phys. Rev. B* **2012**, *86*, 174307.
(71) Li, W.; Carrete, J.; A. Katcho, N.; Mingo, N. ShengBTE: A Solver of the Boltzmann Transport Equation for Phonons. *Comput. Phys. Commun.* **2014**, *185*, 1747–1758.
(72) Hill, R. The Elastic Behaviour of a Crystalline Aggregate. *Proc. Phys. Soc. A* **1952**, *65*, 349–354.
(73) Yu, Y.; Sun, W.-T.; Hu, Z.-D.; Chen, Q.; Peng, L.-M. Oriented Bi_2Se_3 Nanoribbons Film: Structure, Growth, and Photoelectric Properties. *Mater. Chem. Phys.* **2010**, *124*, 865–869.
(74) Rabenau, A. The Role of Hydrothermal Synthesis in Preparative Chemistry. *Angew. Chem., Int. Ed. Engl.* **1985**, *2*, 1026–1040.
(75) Sheets, W. C.; Mugnier, E.; Barnabé, A.; Marks, T. J.; Poeppelmeier, K. R. Hydrothermal Synthesis of Delafossite-Type Oxides. *Chem. Mater.* **2006**, *18*, 7–20.
(76) Shannon, R. D. Revised Effective Ionic Radii and Systematic Studies of Interatomic Distances in Halides and Chalcogenides. *Acta Crystallogr., Sect. A* **1976**, *32*, 751–767.
(77) Yang, L.; Powell, D. R.; Houser, R. P. Structural Variation in Copper (I) Complexes with Pyridylmethylamide Ligands: Structural Analysis with a New Four-Coordinate Geometry Index, τ4. *Dalton Trans.* **2007**, No. 9, 955–964.
(78) Perdew, J. P.; Yang, W.; Burke, K.; Yang, Z.; Gross, E. K. U.; Scheffler, M.; Scuseria, G. E.; Henderson, T. M.; Zhang, I. Y.; Ruzsinszky, A.; Peng, H.; Sun, J.; Trushin, E.; Görling, A. Understanding Band Gaps of Solids in Generalized Kohn–Sham Theory. *PNAS* **2017**, *114*, 2801–2806.
(79) Jaffe, J.; Zunger, A. Theory of the Band-Gap Anomaly in ABC_2 Chalcopyrite Semiconductors. *Phys. Rev. B* **1984**, *29*, 1882.
(80) Xia, Y.; Pal, K.; He, J.; Ozoliņš, V.; Wolverton, C. Particlelike Phonon Propagation Dominates Ultralow Lattice Thermal Conductivity in Crystalline Tl_3VSe_4. *Phys. Rev. Lett.* **2020**, *124*, 065901.
(81) Hermann, R. P.; Grandjean, F.; Long, G. J. Einstein Oscillators That Impede Thermal Transport. *Am. J. Phys.* **2005**, *73*, 110–118.
(82) Pan, L.; Bérardan, D.; Zhao, L.; Barreteau, C.; Dragoe, N. Influence of Pb Doping on the Electrical Transport Properties of BiCuSeO. *Appl. Phys. Lett*. **2013**, *102*, 023902.
(83) Heremans, J. P. The Anharmonicity Blacksmith. *Nat. Phys.* **2015**, *11*, 990–991.
(84) D. Nielsen, M.; Ozolins, V.; P. Heremans, J. Lone Pair Electrons Minimize Lattice Thermal Conductivity. *Energy Environ. Sci.* **2013**, *6*, 570–578.

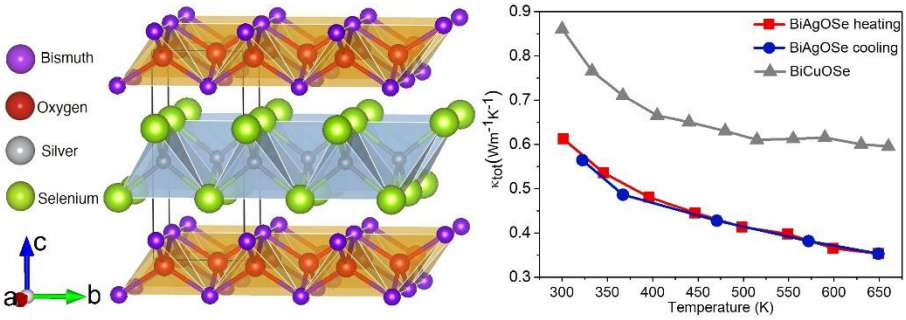
Bismuth
Oxygen
Silver
Selenium
c
a
b
BiAgOSe heating
BiAgOSe cooling
BiCuOSe
κtot(Wm-1K-1)
Temperature (K)
0.9
0.8
0.7
0.6
0.5
0.4
0.3
300
350
400
450
500
550
600
650